

Laser ablation inductively-coupled plasma mass spectrometry (LA-ICP-MS)

Laser ablation analyses were carried out at CODES Analytical Laboratories, University of Tasmania, using a RESolution laser platform, equipped with a Coherent COMPex Pro 193 nm excimer laser and Lauren Technic S155 large format sample cell, coupled to an Agilent 7700 or 7900 quadrupole ICP-MS. The laser operating parameters were optimized for pyrite analysis using a fluence of 2.7 J/cm² and 5 Hz laser repetition rate. Samples were ablated in an atmosphere of pure He flowing through the sample cell at a rate of 0.4 L/min and immediately mixed with ~ 1 L/min Ar in the exit funnel before flowing on to the ICP-MS. The ICP-MS instrument was optimized balancing sensitivity on mid- to high-mass and production of molecular oxide interferences (i.e., ²³²Th¹⁶⁰⁺/²³²Th⁺) and doubly charged ion interferences (i.e., ¹⁴⁰Ce⁺⁺/¹⁴⁰Ce⁺), with both interferences maintained at levels below 0.2%. Many element isotopes were measured to explore trace element contents of the pyrite and to reveal minerals other than pyrite that might be captured during analysis as mineral inclusions within pyrite or in minerals adjacent to pyrite. Concentrations for the following elements hosted within pyrite are reported here: Fe, Co, Ni, Cu, Zn, As, Se, Ag, Sb, Te, Au, Pb and Bi (Table 3). For each spot analysis, the background signal is recorded for 30 seconds, then the laser is turned on and the targeted mineral is ablated while the ICP-MS collects data for each element for ~60 seconds (Fig. 4). During spot analysis, the material analysed is typically dominated by the targeted mineral. Element signals that show no changes, gradual smooth changes, or changes consistent with chemical zonation are interpreted to be chemically bound into the target mineral structure. However, lasering through evenly distributed ‘invisible’ micro-inclusions may also show no or gradual changes in the signal and are therefore indistinguishable from ‘true’ chemical substitution into the mineral structure. Both types

of occurrences are referred to as *refractory*. Elements that have signals with discrete, sharp changes in the laser signal, and can sometimes reach level to dilute target major element signals are interpreted as being hosted in mineral inclusions or in minerals adjacent to the target. To calculate concentrations, the average of the signal over the time interval of interest is calibrated against reference standard STDGL3, an in-house standard sulfide-rich glass for primary calibration for quantifying siderophile and chalcophile elements (after Danyushevsky et al., 2011). Laser spot size is 29 μm for all pyrite and 51 μm for STDGL3 standard glass. The detection limit values (in ppm) are as follows: Mg = 0.53, S = 3800, Ti = 3.72, V = 0.12, Cr = 1.94, Mn = 0.82, Co = 0.1, Ni = 0.2, Cu = 0.5, Zn = 0.97, As = 0.53, Se = 8, Zr = 0.003, Nb = 0.04, Mo = 0.11, Ag = 0.05, Cd = 0.19, Sn = 0.11, Sb = 0.1, Te = 0.66, Gd = 0.14, Hf = 0.06, Ta = 0.02, W = 0.06, Au = 0.04, Tl = 0.02, Pb = 0.02, Bi = 0.02, Th = 0.03, U = 0.02, Al = 0.28, and Hg = 45.36.

Imaging of pyrite

LA-ICP-MS imaging was carried out by ablating sets of parallel lines in a grid across the minerals in the samples. Depending on the target mineral size, lines were ablated with a beam size of 7 or 11 μm translated at 7 and 11 $\mu\text{m/s}$, respectively. The spacing between the lines was kept constant at the same size as the laser beam. The lines were ablated with the repetition rate of 10 Hz, thus, every position in the sample was ablated 10 times and its composition contributed to 5 consecutive pixels in the image, resulting in an unprocessed effective resolution matching the beam size. Every sweep recorded in the mass spectrometer forms a separate pixel in the map. Depth of ablation during mapping was < 3 μm . A set of 41 element isotopes were analyzed: ^{23}Na , ^{24}Mg , ^{27}Al , ^{29}Si , ^{34}S , ^{39}K , ^{43}Ca , ^{49}Ti , ^{51}V , ^{53}Cr , ^{55}Mn , ^{57}Fe , ^{59}Co , ^{60}Ni , ^{65}Cu , ^{66}Zn , ^{75}As , ^{77}Se , ^{90}Zr , ^{95}Mo , ^{107}Ag , ^{109}Ag , ^{111}Cd , ^{118}Sn , ^{121}Sb , ^{125}Te , ^{137}Ba , ^{157}Gd , ^{178}Hf , ^{181}Ta , ^{182}W , ^{195}Pt , ^{197}Au , ^{202}Hg , ^{205}Tl , ^{206}Pb , ^{207}Pb , ^{208}Pb , ^{209}Bi , ^{232}Th and ^{238}U . Background levels and the primary sulfide standard (STDGL3;

after Danyushevsky et al., 2011) were measured before and after each image. Data reduction and processing for the laser images were performed using CODES in-house routines.

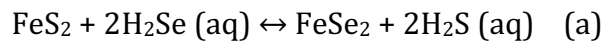
Sericite $^{40}\text{Ar}/^{39}\text{Ar}$ dating

The sericite sample (HL-98), collected from argillic alteration zone (stage V), was used for $^{40}\text{Ar}/^{39}\text{Ar}$ dating. Before $^{40}\text{Ar}/^{39}\text{Ar}$ analysis, mineral separation was performed by crushing, sieving and handpicking at the Langfang Geochemical Laboratory in Hebei, China. In order to ensure > 99% purity of the selected sericite, examination using a binocular microscope was performed. To minimize nuclear interference reactions, the selected sericite grains were loaded into a 1.9 cm in diameter and 0.3 cm deep aluminum disc during irradiation. The $^{40}\text{Ar}/^{39}\text{Ar}$ analysis was performed at the Western Australian Argon Isotope Facility, Curtin University. The detailed information of the analytical procedure can be found in Jourdan et al. (2014), and the raw data were processed using the ArArCALC software (Koppers, 2002). The plateau age was defined by over a minimum of three consecutive steps that contained more than 50% of the released ^{39}Ar , agreed at the 95% confidence level and satisfied a probability of fit (P) of at least 0.05. Where no plateau age behavior was identified, a weighted-mean age is given. Mean J-value computed from the monitor mineral is $0.01080000 \pm 0.00001890$. The plateau age errors were within the 2σ level and were calculated using the mean of all plateau steps, in which each step was weighted by the inverse variance of its individual analytical error. An integrated age (2σ) was also calculated by combining the results from all steps of the incremental heating analysis.

Se contents in pyrite and implication for fluid Se/S ratios

When H_2Se and H_2S are the dominant aqueous Se and S species, $m_{\text{H}_2\text{Se}}/m_{\text{H}_2\text{S}}$ can

represent $m_{\Sigma \text{Se}}/m_{\Sigma \text{S}}$ and the partition of Se between hydrothermal and coexisting pyrite will be expressed as a generalized reaction as suggested by Huston et al. (1995):



For diluted hydrothermal and ideal solid solutions, the activity of ferroselite (a_{FeSe_2}) and pyrite (a_{FeS_2}) approximates X_{Se}^2 and X_{S}^2 , respectively, with the activity coefficients remaining near unity. Therefore, reaction coefficient (K) is expressed as follows:

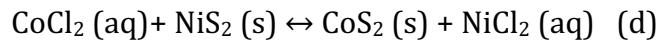
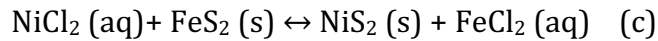
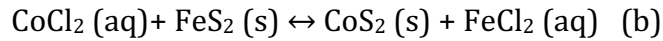
$$K_a = [(m_{\text{Se}}/m_{\text{S}})_{\text{pyrite}} / (m_{\text{H}_2\text{Se}}/m_{\text{H}_2\text{S}})_{\text{fluid}}]^2$$

Since $K = \text{EXP}(-\Delta G/RT)$ and $\Delta G = \Delta G^o - \int_{T^o}^T [\Delta S_{T^o} + \int_{T^o}^T \frac{\Delta C_p}{T} dT] dT$ where ΔG refers to the change of Gibbs free energy, ΔS refers to entropy change of the reaction, and ΔC_p refers to heat capacity of the reaction under constant pressure. Based on the necessary thermodynamic data of FeSe_2 , FeS_2 , H_2S , and H_2Se provided by Huston et al. (1995), the dependence of Se incorporated into the pyrite lattice as stoichiometric substitution on temperature and ratios of $\text{H}_2\text{Se}/\text{H}_2\text{S}$ in fluid are shown in Figure 11a.

A key factor affecting the participation of Se is the assumption of using $m_{\text{H}_2\text{Se}}/m_{\text{H}_2\text{S}}$ to represent $m_{\Sigma \text{Se}}/m_{\Sigma \text{S}}$, which may be inadequate when native Se is present in hydrothermal system (Huston et al., 1995). However, the range of native Se shrinks with increasing temperature, eventually disappearing at around 200 °C (Appendix 4). Consequently, this safely rules out the uncertainty induced by the presence of native Se. The dependence of ΔG on pressure can also be safely ignored, since no gases are involved in the reaction. Moreover, as revealed by fluid inclusion analysis in this study that the Yulekenhalasu deposit was formed in relative shallow level (<2 km depth), it is safe to ignore the influence of high pressures on the calculation.

Co and Ni levels in pyrite and implication for fluid Co/Ni ratios

The partition of Co and Ni between hydrothermal and coexisting pyrite are first established as a series of generalized reactions:



For ideal solid solutions, the mixing on site model considers the substitution of species in any site individually; hence, the activity of pyrite (a_{FeS_2}), cattierite (a_{CoS_2}), and vaesite (a_{NiS_2}) approximates X_{Fe} , X_{Co} , and X_{Ni} in corresponding sulfides, respectively. As the activity coefficients for CoCl_2 , NiCl_2 , and FeCl_2 are near to unity, equilibrium constants (K) for the reactions are expressed as follows:

$$K_b = (m_{\text{Co}}/m_{\text{Fe}})_{\text{pyrite}} / (m_{\text{CoCl}_2}/m_{\text{FeCl}_2})_{\text{fluid}}$$

$$K_c = (m_{\text{Ni}}/m_{\text{Fe}})_{\text{pyrite}} / (m_{\text{NiCl}_2}/m_{\text{FeCl}_2})_{\text{fluid}}$$

$$K_d = (m_{\text{Co}}/m_{\text{Ni}})_{\text{pyrite}} / (m_{\text{CoCl}_2}/m_{\text{NiCl}_2})_{\text{fluid}}$$

Based on thermodynamic data for FeS_2 , NiS_2 , CoS_2 , CoCl_2 , NiCl_2 , and FeCl_2 provided by Reed (1989), Barin (1995), Yungman et al. (1999), Holland and Powell (2011), Barin et al. (1977), the dependence of Ni and Co incorporated into the pyrite lattice as stoichiometric substitution on temperature and ratios of Co/Ni in fluid are constructed in Figure 11.

Although the assumption of using neutral chloride complexes (CoCl_2 , NiCl_2 , and FeCl_2) to represent the metal species in the fluid seems arbitrary, experiments and theoretical considerations suggest that neutral species should be favored in the lower pressure, higher temperature realm of the supercritical region (Arancibia and Clark, 1996; Chou and Eugster, 1977; Ilton and Eugster, 1989; Simon et al., 2004). Moreover, since hydrothermal fluid at the Yulekenhalasu deposit has been proved to be a $\text{NaCl-H}_2\text{O}$

dominated system (Yang et al., 2012), combined with the preferential nature of Co, Ni and Fe to form chloride complexes, our calculations should be suitable in order to roughly constrain Ni and Co proportions in hydrothermal fluids at Yulekenhalasu.

References:

- Arancibia, O.N., and Clark, A.H. (1996) Early magnetite-amphibole-plagioclase alteration-mineralization in the Island Copper porphyry copper-gold-molybdenum deposit, British Columbia. *Economic Geology*, 91(2), 402–438.
- Barin, I. (1995) Thermochemical data of pure substances. 1885 p. VCH Verlags Gesellschaft, Weinheim.
- Barin, I., Knacke, O., and Kubaschewski, O. (1977) Thermochemical properties of inorganic substances: supplement. 861 p. Springer-Verlag Berlin Heidelberg.
- Chou, I.M., and Eugster, H.P. (1977) Solubility of magnetite in supercritical chloride solutions. *American Journal of Science*, 277(10), 1296–1314.
- Holland, T.J.B., and Powell, R. (2011) An improved and extended internally consistent thermodynamic dataset for phases of petrological interest, involving a new equation of state for solids. *Journal of Metamorphic Geology*, 29(3), 333–383.
- Huston, D.L., Sie, S.H., Suter, G.F., Cooke, D.R., and Both, R.A. (1995) Trace elements in sulfide minerals from eastern Australian volcanic-hosted massive sulfide deposits; Part I, Proton microprobe analyses of pyrite, chalcopyrite, and sphalerite, and Part II, Selenium levels in pyrite; comparison with delta ^{34}S values and implications for the source of sulfur in volcanogenic hydrothermal systems. *Economic Geology*, 90(5), 1167–1196.
- Ilton, E.S., and Eugster, H.P. (1989) Base metal exchange between magnetite and a chloride-rich hydrothermal fluid. *Geochimica et Cosmochimica Acta*, 53(2), 291–301.
- Jourdan, F., Mark, D.F., and Verati, C. (2014) Advances in $^{40}\text{Ar}/^{39}\text{Ar}$ dating: From archaeology to planetary sciences. Geological Society of London.
- Koppers, A.A.P. (2002) ArArCALC-software for $^{40}\text{Ar}/^{39}\text{Ar}$ age calculations. *Computers & Geosciences*, 28(5), 605–619.
- Reed, J.J. (1989) The NBS tables of chemical thermodynamic properties: selected values for inorganic and C1 and C2 organic substances in SI units. National Institute of Standards and Technology.
- Simon, A.C., Pettke, T., Candela, P.A., Piccoli, P.M., and Heinrich, C.A. (2004) Magnetite solubility and iron transport in magmatic-hydrothermal environments. *Geochimica et Cosmochimica Acta*, 68(23), 4905–4914.
- Yungman, V.S., Glushko, V.P., Medvedev, V.A., and Gurvich, L.V. (1999) Thermal constants of substances, 8 volume set. Wiley, New York.